Research article

MoS$_2$ nanoflower decorated bio-derived chitosan nanocomposites for sustainable energy storage: Structural, optical and electrochemical studies

Muhammad Rakibul Islam [*], Homaira , Eashika Mahmud , Rabeya Binta Alam

Nanocomposite Research Laboratory, Department of Physics, Bangladesh University of Engineering and Technology (BUET), Dhaka, Bangladesh

A B S T R A C T

Bio-derived chitosan-molybdenum di sulfide (Cs–MoS$_2$) nanocomposites are prepared by a simple and economical aqueous casting method with varying concentrations of MoS$_2$. The structural, surface morphological, optical, and electrochemical properties of the nanocomposites were studied. FTIR analysis reveals the strong interaction between Cs and MoS$_2$. FESEM micrograph showed an increment of the surface roughness due to the incorporation of MoS$_2$ layers into Cs. The surface wettability of the nanocomposites was found to be decreased from 73° to 33° due to the incorporation of MoS$_2$ into the chitosan. UV–vis spectroscopy study demonstrates a reduction of optical bandgap from 4.29 to 3.44 eV as the nanofiller, MoS$_2$, introduces localized states within the forbidden energy bandgap. The incorporation of MoS$_2$ was found to increase the specific capacitance of Cs from 421 mFg^{-1} to 1589 mFg^{-1} at a current density of 100 μAg^{-1}. The EIS analysis revealed an increase in the pseudo-capacitance from 0.09 μF to 4.13 μF and a reduction of charge transfer resistance that comes from the nanofiller contribution. MoS$_2$ nanoflower introduces more active sites and expands the electroactive zone, thus improving the charge storage property of Cs. The Cs–MoS$_2$ may offer a new route for the synthesis of eco-friendly, biodegradable, and electrical storage devices.

1. Introduction

The global energy demand is rising rapidly across the industrial sectors, urban life, transportation, etc., due to the rapid development of modern society, the economy, and the ongoing population growth [1,2]. As a result, increased amounts of non-renewable energy sources like oil, fossil fuels, and natural gas have been consumed, causing the depletion of energy resources, becoming a significant challenge for a sustainable energy future [3,4]. Renewable energy sources directly generated from the solar system, air, hydroelectric, biomass, and other natural atmospheric activities (such as geothermal and tidal energy) need to be stored up to mitigate the problem [4,5]. Electrochemical energy storage devices, such as supercapacitors and rechargeable batteries, have developed quickly as energy storage for many newly developed technologies due to their ability to supply satisfactory results, excellent security, and longer service life [6,7]. Though supercapacitors have a lower energy density compared to batteries, they can charge and discharge quickly. Also, they can withstand hundreds of thousands to millions of charge-discharge cycles without significant degradation, reducing long-term maintenance costs [8,9]. This is the reason many research areas are emphasized on supercapacitors. However,

---

research in energy storage is not solely focused on supercapacitors over batteries; both supercapacitors and batteries have active and valuable areas of energy storage materials research. The most effective electrode materials for energy storage are often made of noble metals (such as Pt, Au, Pd, etc.). Still, their limited availability and high price severely confined their use in practical applications [10, 11]. The large-scale manufacture and use of cathode materials based on transition metals (TMs) (such as Mn, Fe, Co, and Ni) raise concerns about the depletion of non-renewable mineral resources and environmental issues such as soil and water contamination as they are a potential source of electronic waste, even though these materials display higher energy storage capacity [12,13].

It has received much support in recent years to create polymer electrodes based on biodegradable polymers such as cellulose, starch, agar, and carrageenan, which help to lessen the adverse effects of harmful items on the environment [14,15]. Chitosan (Cs) is considered one of the most abundant biopolymers and is a linear polysaccharide made up of N-acetyl-D-glucosamine and b-(1–4)-linked-D-glucosamine [16,17]. It is produced by alkaline deacetylating chitin, found in the exoskeleton of marine creatures, including shrimp, crabs, and lobsters [18]. Cs, an eco-friendly substance with cheap manufacturing costs, has received significant acceptance in fields like water treatment, food packaging, tissue engineering, constructing sensors, and pharmaceutical medication delivery because of its consistent biocompatibility, biodegradability, high permeability, minimal immunogenicity, antibacterial qualities, beneficial optical characteristics, and better film-forming capacity [19–23]. The greatly delocalized, polarized, and electron-dense π bonds that compose form a conjugated carbon chain's interchanging single and double bonds are what leads to better optical properties of Cs. The nitrogen and hydrogen atoms in the amine and hydroxyl functional groups of Cs have lone-pair electrons, which are required for a polymer electrode system since they will produce synchronization interconnections with the charged particles [24]. As a result of the ongoing interactions of the charge carriers with the accessible, functional group, the polymer chain segment transportation will be produced, making the polymer have conductive behavior. However, it is low [25], the reason for low conductivity is due to the rigidly bounded hydrogen atom in Cs. The Cs membranes can retain and absorb a substantial volume of solution (water or electrolyte). This characteristic makes it possible for Cs membranes to have ionic mobility, which is essential for electrochemical applications [26]. One disadvantage of employing Cs as an electrode appears to be its low conductivity. A further downside is that with prolonged use, organic liquid solvent leakage from the Cs electrode may occur, reducing the ionic conductivity [27]. Another disadvantage is that it has weak chemical resistance where amino and hydroxyl groups in Cs are vital in raising the resistance of electrodes by disrupting anions and bulky substances [28].

The above-mentioned issues can be solved by adequately dispersing inorganic fillers with sizes of nano or submicron into the polymer. It has also been demonstrated that fillers may significantly affect the characteristics of polymer electrodes. Inorganic fillers can be added to materials to prevent the crystallization of the polymer, which enhances ion movement during the morphological phase and increases the electrochemical stability at the interfacial interface [29]. Particularly, transition-metal dichalcogenides (TMDs), such as MoS_2, SnS_2, and WS_2, have drawn much interest in various fascinating applications due to their superior mechanical and electrical properties, high spin-orbit coupling, modified bandgap, atomic scale thickness, catalyst properties [30], charge storage capabilities [31] and other distinguishing features [32]. Within the array of TMDS nanofillers available, nanostructured MoS_2 has garnered significant attention as a filler material for nanocomposites. This preference is due to its outstanding attributes, as it demonstrates a substantial surface area, and unique stacked structure characterized by strong covalent bonds, microwave absorption, better hydrophilicity, stronger electrical conductivity, and higher intrinsic fast ionic conductivity [33,34]. MoS_2 has also gained research attention as the remedy of the hazardous behavior of some other TMs [35,36].

In this study, we employed a straightforward and cost-effective method involving aqueous casting to synthesize a nanocomposite consisting of Cs–MoS_2. The solution casting technique offers a practical and economical route for generating large-scale nanocomposites based on polymers, which hold promise for various industrial applications [37]. The unique attributes of the nanocomposite films were investigated using Fourier-transform infrared (FTIR) spectroscopy, field emission scanning electron microscopy (FESEM), measurements of surface wettability, and evaluation of optical characteristics. The capacitive properties were evaluated using cyclic voltammetry, galvanostatic charging-discharging techniques, and electrochemical impedance spectroscopy (EIS) analysis using an equivalent AC circuit. Notably, improvements in specific capacitance were observed (rising from 421 mFg^{-1} to 1589 mFg^{-1} at 100 μAg^{-1}) alongside a decrease in contact resistance, as demonstrated by the electrochemical analysis. This eco-friendly electrode material, derived from natural sources, devoid of hazardous components, and capable of biodegradation, exhibits enhanced energy storage capabilities. The comprehensive exploration of this bio-inspired material possessing enhanced electrochemical attributes could find utility in the realm of flexible, environmentally friendly, next-generation electronic devices.

2. Materials

Chitosan (extra pure, 90 %, Loba Chemie, India), sodium molybdate dehydrates ($Na_2MoO_2 \cdot 2H_2O$) (98 %, Merck, Germany), thiourea (CH_4N_2O) (98 %, Research-Lab, India), and glycerol (98 %, Loba Chemie, India). All of the chemicals were used in their original condition without any purification.

2.1. Synthesis of MoS_2

The MoS_2 nanoflower was synthesized by hydrothermal method. Sodium molybdate dihydrate ($Na_2MoO_4 \cdot 2H_2O$) was required as the source for molybdenum (Mo), and (CH_4N_2S) was the sulfur (S) source. Initially, sodium molybdate dihydrate and thiourea were dissolved in 120 ml of distilled water, followed by vigorous stirring, which produced a transparent solution. The solution was then transferred into a 200 mL Teflon-lined autoclave and hydrothermally treated for 24 h at 200 °C. The precipitate was centrifuged and then rinsed using ethanol and di-ionized (DI) water. The obtained black powder was dried at 60 °C for a couple of hours to achieve

MoS$_2$ nanoflower [38].

2.2. Preparation of nanocomposite

The Cs–MoS$_2$ nanocomposite film was prepared through the solution casting method, where MoS$_2$ concentrations were varied, ranging from 0.1 wt% to 0.5 wt%. Initially, a base solution, the Cs solution, was created by dissolving 1.5 gm of Cs in a 1 % acetic acid aqueous solution, with vigorous mechanical stirring performed at room temperature. In the meantime, a dopant solution of MoS$_2$ was prepared, involving the addition of 15 mg of MoS$_2$, 15 ml of deionized water, and 3 ml diluted Cs solution. This Cs diluted solution was prepared with a minute amount of Cs and 3 ml of 1 % acetic acid. The agglomeration of MoS$_2$ is very common and tends to become sediment at the bottom of the beaker [39]. Therefore, to ensure good dispersibility, and stability, a diluted Cs solution was added with the dopant solution. Cs, as a surfactant, provides the hydroxyl, carboxyl, and amino groups that cover the surface of MoS$_2$ and provide homogeneous dispersion by reducing the possibilities of MoS$_2$ aggregation. Then, to prepare the film, the required amount of dopant solution was added into the base solution with the help of a pipette and stirred using a magnetic stirrer at 45 °C 5 ml glycerol was added to this total solution to thicken the solution. Here, to mention, the diluted Cs solution is so less in amount that it doesn't affect the overall composite concentration. Then, when the solution was thick enough to form a film, it was poured into a Petri dish and left dried at room temperature until the film was formed. The film was then carefully peeled from the Petri dish when sufficiently dry and preserved for subsequent characterization. In this case, the samples with 0, 0.1, 0.3, and 0.5 % of MoS$_2$ with Cs are referred to as samples A, B, C, and D respectively.

2.3. Characterization techniques

Fourier transform infrared spectroscopy (FTIR) investigation was carried out using a (Shimadzu IRSpirit) spectrophotometer to investigate the nanocomposite chemical structure. The surface morphology of the nanocomposites was examined under a 5 kV accelerating voltage using a field emission scanning electron microscopy (FESEM) (JEOL JSM-7600F). The contact angle (CA) was determined to evaluate the surface wettability by maintaining optimized circumstances and adjusting humidity using a contact angle meter (Apex, India) where the sessile drop technique had been employed. To measure the CA using the tangential method, 10 μL DI water was dropped onto the surface of the films. Each reported contact angle data was determined by averaging the values of three independent readings. The optical band gap of nanocomposite film was analyzed by utilizing a UV–vis Spectrophotometer (UV-2100), keeping the wavelength region between 190 and 800 nm. The electrochemical performance was performed at room temperature using a CS310 electrochemical working station (Corrtest, China). The investigations were carried out using an electrochemical chamber with three electrodes and an operating electrode made of glassy carbon. A platinum plate (1 × 1 cm^2), a silver/silver chloride electrode (Ag/AgCl), and 0.5 M Na$_2$SO$_4$ were used as a counter electrode, reference electrode, and an ionic electrolyte solution, respectively.

3. Results and discussions

3.1. Chemical bond analysis

FTIR analysis was carried out to understand the structural changes that may occur among the chitosan polymer due to the incorporation of MoS$_2$ nanoflower. Fig. 1 shows the FTIR spectra for Cs and Cs–MoS$_2$ nanocomposites. From the FTIR spectra of Cs, a broad band in the ranges between 3000 cm^{-1} and 3700 cm^{-1} conforms to the symmetric bending vibration of the hydroxyl and the
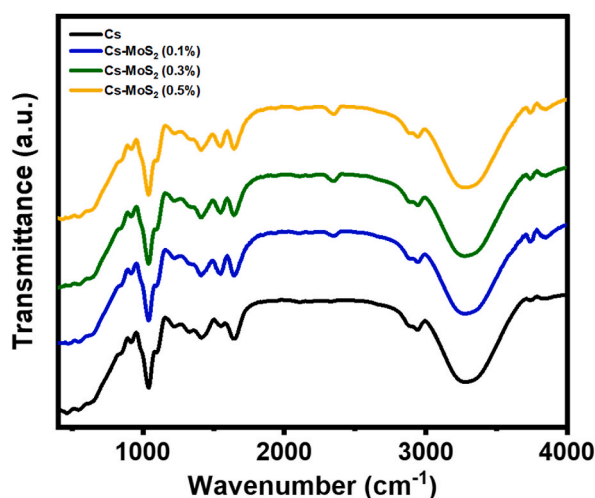

Fig. 1. FTIR spectrum of Cs–MoS$_2$ nanocomposites for different concentrations of MoS$_2$ nanoflower.

amine units, suggesting the development of intra- and intermolecular H-bonds between the hydroxyl and amine units [40,41]. The absorption bands at around 2942 cm^{-1} and 2894 cm^{-1} can be attributed to alkane units' C–H symmetric and asymmetric stretching vibration, respectively [42,43]. The peak at 1652 cm^{-1} cm can be ascribed to the C=O stretching vibration of amide I [34]. The spectrum at 1548 cm^{-1} is representative of the bending vibration of amide II, a frequent peak of Cs [44]. The band at 1420 cm^{-1} corresponds to the stretching vibration of C–O and 1330 cm^{-1} to the C–N stretching of amide III representing residual N-acetyl [45]. The peak at 1100 cm^{-1} is designated to the asymmetric stretching vibration of the C–O–C bridge and 1035 cm^{-1} to the C–O stretching in polysaccharide units [456]. The FTIR spectra at 920 cm^{-1} are attributed to the C–O stretching of the glycoside linkage N–H (amide III) ring stretching [32].

There are no observable new peaks in the Cs–MoS$_2$ nanocomposites observed. Since a very low concentration of MoS$_2$ nanofiller was used and that may be absorbed in polymer matrix, thus, the bonding with Mo or S is not observed. The increase in the amplitude of the N–H bending vibration is caused by the weak or insignificant noncovalent contact between the chitosan and MoS$_2$ nanoparticle. A gradual increase in the amplitude of the band for –OH stretching vibration is also observed, indicating the formation of new intra-molecular H-bonds, which can be attributed to the increase of the nanoflower in the nanocomposites. The characteristics found in the FTIR provide evidence of the presence of Cs–MoS$_2$ nanoflower interactions.

3.2. Surface morphology analysis

The surface morphology of Cs, MoS$_2$ nanoflower, and Cs–MoS$_2$ nanocomposite film was investigated using FESEM, and the resulting images are presented in Fig. 2(a)-(e). Fig. 2(a) illustrates the FESEM images of Cs film, demonstrating a smooth and uniform surface without any pores throughout the film. The FESEM image of a MoS$_2$ nanoflower with several nanoscale petals is shown in Fig. 2 (b). It shows that the petals are irregularly connected and closely arranged into a shared center, developing the appearance of a spherical flower. Furthermore, the observed porous structure of MoS$_2$ nanoflowers has a great influence on the electrochemical performance of the nanocomposites. Fig. 2(c)–(e) represents the FESEM images of Cs–MoS$_2$ for different concentrations of MoS$_2$ nanofiller, which confirms the presence of MoS$_2$ nanoflower by the appearance of the petals entrapped with Cs. Cs–MoS$_2$ nano-composite films exhibit significantly more noticeable pores, which are objective to the formation of MoS$_2$ nanoflower on the surface. The porous structure allows an increased number of ion particles to come to the surface of the active materials. The incorporation of MoS$_2$ furthermore increases the surface roughness of the films, which also increases the surface area. An increase in surface will allow more active sites to come to the surface area and help improve the electrochemical performance.

3.3. Surface wettability

The wettability of a film, which is influenced by its topology and chemical composition, significantly impacts the potential uses of bio-nanocomposite materials. A substrate's contact angle (CA) is a reliable measure of its wettability. Fig. 3 shows the variation in CA with the different concentrations of MoS$_2$ incorporated in chitosan composite, and the CA of the materials reduces with the increase of the concentration of MoS$_2$ nanoflower. The measured CA of Cs was obtained at 73°, denoting hydrophilic behavior, which is attributed to the –OH and –NH$_2$ bond of Cs. The CA was found to be reduced from 73° for Cs to 33° for Cs–MoS$_2$ (0.5 %) nanocomposite film. As a smaller CA denotes a higher hydrophilicity of the surface, it appears that the incorporation of MoS$_2$ nanoflower into Cs increases the hydrophilicity of the material. This behavior may be attributed to the accessible sulfur molecules in MoS$_2$ nanoflower that cause the
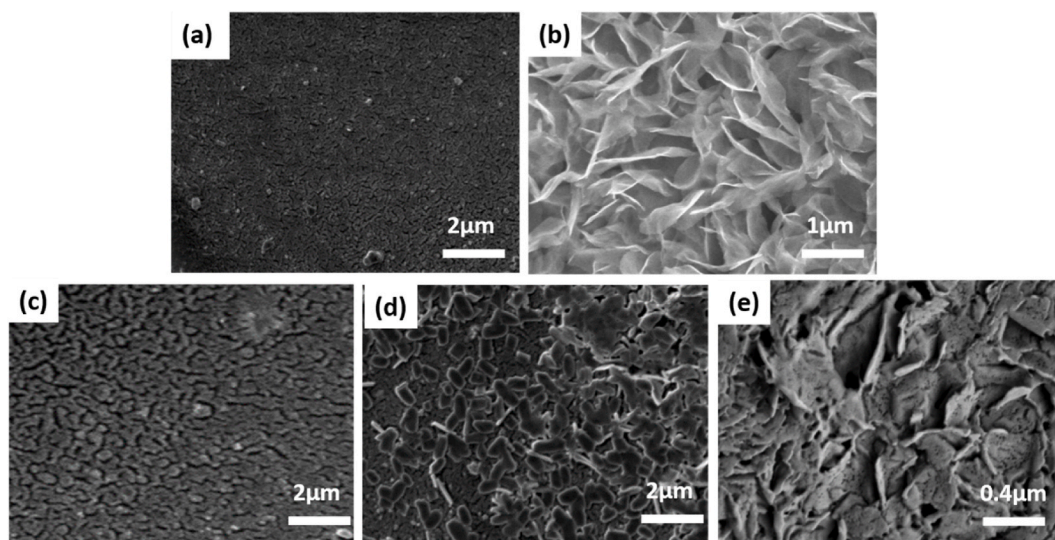

Fig. 2. FESEM images of (a) Cs (b) MoS$_2$ nanoflower, (c) Cs–MoS$_2$ (0.1 %) (d) Cs–MoS$_2$ (0.3 %), and (e) Cs–MoS$_2$ (0.5 %) nanocomposites.
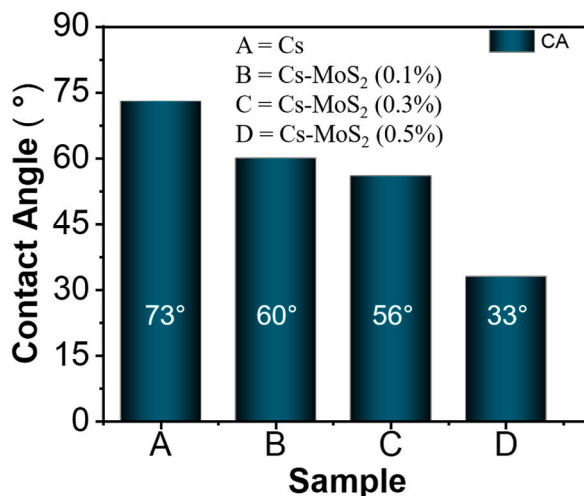
Fig. 3. Contact angle (CA) of as-prepared Cs–MoS$_2$ nanocomposites, where MoS$_2$ concentration were varied.

entire surface to be hydrophilic, giving the nanocomposite a high liquid attraction by conducting hydrogen bonding. The enhanced hydrophilic nature of the composite allows for better electrolyte penetration, enhances active sites, and thereby improves capacitive performance. Furthermore, modification of the surface morphology can also influence wettability. From the FESEM images, it is evident that the incorporation of MoS$_2$ nanoflower increases the roughness of the film. The enhanced roughness increases the surface's hydrophilic nature as it expands the surface area of interaction between water and nanocomposite film. We may, therefore, assume that the increase in surface roughness and sulfur molecules are both correlated to the reduction in water CA. The appearance of morphology resembling petals on the nanocomposite films due to the addition of MoS$_2$ nanoflower, demonstrated by the FESEM analysis, may affect the surface wettability [36].

3.4. Optical properties

The optical properties of the nanocomposites were studied using UV–vis spectroscopy. Fig. 4 (a,b,c and d) shows the $(\alpha h\upsilon)^2$ vs. $h\upsilon$ curve for different nanocomposites that reveal their optical band gap. The intercept of the linear part of the $(\alpha h\upsilon)^2$ against $h\upsilon$ plots on the *x-axis* was used to estimate the band gap (E_g) values [37]. The band gap energy for Cs is found to be 4.29 eV, which reduces to 3.44 eV for the incorporation of just 0.5 % MoS$_2$. Fig. 4 (e) represents the variation of the E_g for different concentrations of MoS$_2$. The
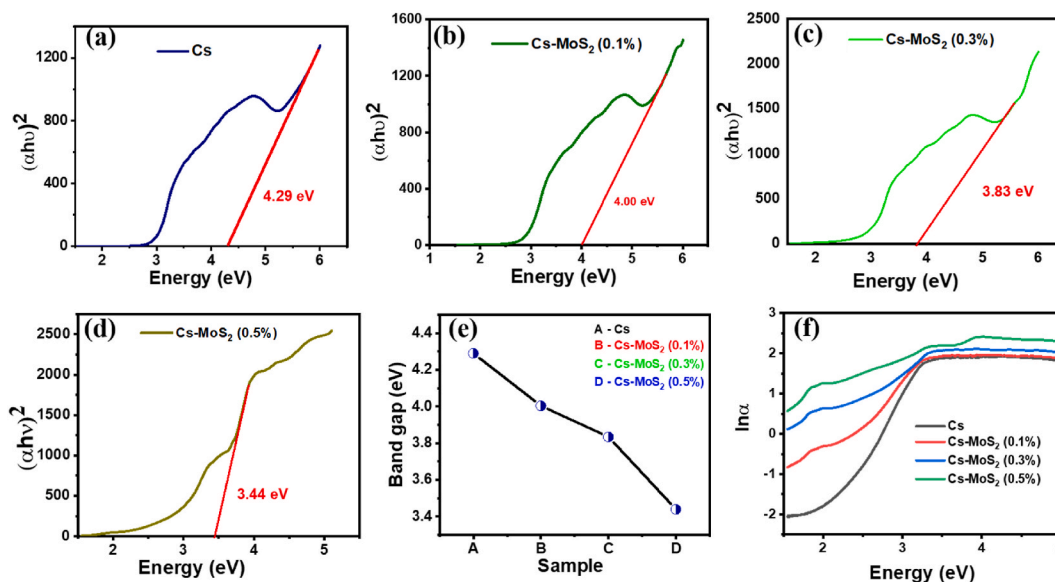

Fig. 4. (a)–(d) The optical band gap energy curve of Cs–MoS$_2$ nanocomposites, (e) variation of the optical bandgap of different samples, and (f) plot of ln (α) vs energy to evaluate of the Urbach energy of Cs–MoS$_2$ nanocomposites.

electron movement in amorphous and polymeric materials may be affected by the localized state due to the shortage of long-range order in these materials. So, a localized state arises between the conduction band and the valence band in addition to the band gap. On the other hand, the S atoms in MoS_2 nanoflower generate p states, providing energies similar to the p-d hybridized states towards the upper part of the valence band. Consequently, the electronic states are localized on both the leading edge of the valence band and the lowest part of the conduction band. As a result of this, MoS_2 nanoflower exhibits a low energy band gap. This reduction in optical band gap can be attributed to the complex that forms due to nanoparticles interacting with the polymer matrix by increasing the density of defects or particle clusters. The rise in the density of defects may enlarge the valence band by arising band tailing inside the forbidden gap of the polymeric system. Moreover, MoS_2 nanoflower may develop localized electronic states within the band gap of Cs, which function as recombination and trapping sites.

To further investigate the role of MoS_2 nanoflower on the optical properties of the polymer, the Urbach energy of all the samples was studied. The defects produce an absorption tail that spreads inside the forbidden gap in the absorption spectrum. The Urbach energy is correlated to this absorption tail, referred to as the Urbach tail [47]. The Urbach energy is also associated with localized states of amorphous structure in amorphous materials [48]. Nanocomposite materials typically show Urbach energy in the forbidden gap due to disordered atoms in the amorphous phase. The spread of energy bands lessens the material's optical bandwidth [49]. The development of the absorption edge at the bandgap energy is caused by either electron-phonon interaction or exciton-phonon interaction [50]. The formula for estimating Urbach energy is

$$\alpha(v) = \alpha_0 \, exp \left(\frac{hv}{E_u} \right)$$

where α_0 is a constant, hv is photon energy, and E_u is the Urbach energy [51]. To estimate the E_u, the natural logarithm of the absorption coefficient $\alpha(\nu)$ was plotted as a function of the photon energy (hv) for the Cs–MoS_2 nanocomposite films and is presented in Fig. 4(f). The Urbach energy was calculated from the inverse of the slope of the linear portion of the $ln(\alpha)$ vs. hv curve. The value of E_u for Cs and Cs–MoS_2 nanocomposite films are shown in Table 1. It is observed that the addition of MoS_2 increases the Urbach energy of nanocomposite films (Fig. 4(b)). Since Urbach energy is a measure of the amorphousness due to inhomogeneous disorders in the materials the observed increase of Urbach energy suggests that the incorporation of MoS_2 introduces localized states within the forbidden energy bandgap [48]. The appearance of new energy levels can influence the transfer of electrons from the valence bands to the conduction band. Moreover, the unsaturated defects increased the density of localized states, resulting in a reduction in the optical energy gap.

3.5. Electrochemical properties

Cyclic voltammetry (CV) investigations were performed to analyze the electrochemical characteristics of the obtained Cs–MoS_2 composites at various scan rates (5–100 mVs^{-1}) in 0.5 M Na_2SO_4 solution within a potential window between -0.2 V and 0.3 V by manufacturing electrodes wrapped with thin layers of composites are shown in Fig. 5(a)-5(d). At a low scan rate, the CV curves of Cs–MoS_2 exhibit a nearly rectangular pattern. With the increase in scan rate, the CV curves diverge from the rectangular shape and become symmetric, indicating ideal capacitive behavior and high-rate capability [52]. Moreover, the CV curves become more quasi-rectangular with the increase in scan rate, signifying convenient capacitive response and speedy charge-discharge performance. It tends to be ascribed to the fact that MoS_2 offers accessible channels to fast ion diffusion and bountiful areas for ion adsorption; Fig. 5 (e) depicts the cyclic voltammetry (CV) curve of the Cs–MoS_2 with various concentrations of MoS_2 at a scan rate of 100 mVs^{-1}. The area of the CV curves for the Cs–MoS_2 electrode is considerably getting wider with the gradual incorporation of MoS_2 nanofiller, indicating the increased active surface area for charge transfer between the electrode and the electrolyte. Thus, the gradual increase in the area of the CV curve with the concentration of MoS_2 nanofiller suggests an increment of the specific capacitance.

The galvanostatic charge-discharge (GCD) studies were performed to evaluate more accurate capacitive performance, where the potential region was determined by considering the CV curves. Fig. 5(f) represents the GCD curves for the Cs–MoS_2 composites at a current density of 100 μAg^{-1} within a potential range of -0.2 V–0.3 V. The symmetry observed in the GCD plots suggests a reversible charge-discharge mechanism of the Cs–MoS_2 nanocomposite. The GCD curve patterns for all the samples closely resemble ideal triangle graphs with minimal deviation, which indicates pseudocapacitive influence [53]. The GCD curve for Cs–MoS_2 (0.5 %) becomes noticeably distorted from the ideal triangle shape, indicating additional pseudocapacitive behavior.

The specific capacitance of the nanocomposites can be determined from the GCD curves using the formula:

$$C_s = \frac{I \Delta t}{m \Delta v}$$

Table 1
Band gap, and Urbach energy of Cs and Cs–MoS_2 nanocomposite.

Sample	Band gap (eV)	Urbach energy (eV)
Cs	4.29	0.279
Cs–MoS_2 (0.1 %)	4.00	0.405
Cs–MoS_2 (0.3 %)	3.83	0.827
Cs–MoS_2 (0.5 %)	3.44	1.429
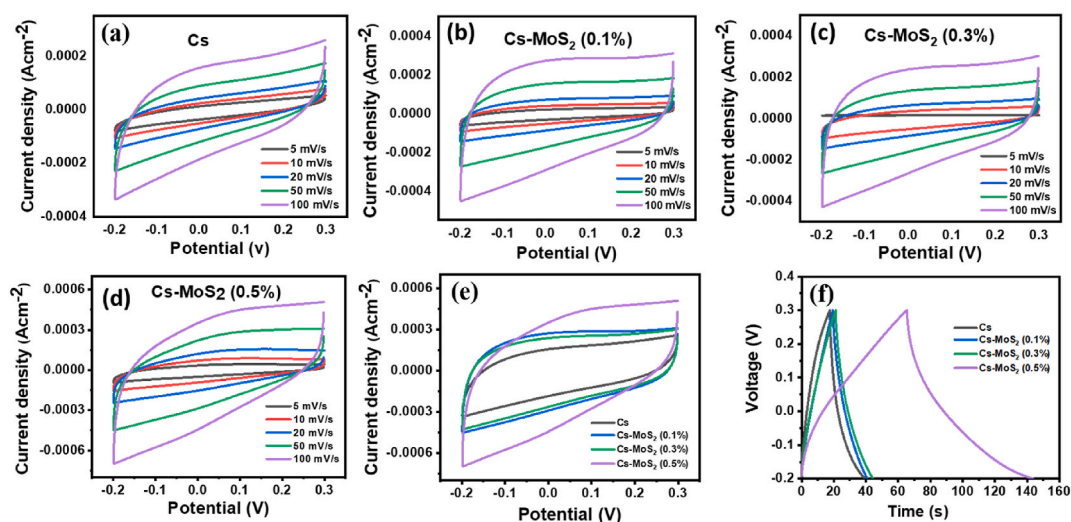
Fig. 5. Cyclic voltammetry of (a) Cs, (b) Cs–MoS$_2$ (0.1 wt%) (c) Cs–MoS$_2$ (0.3 wt%), (d) Cs–MoS$_2$ (0.5 wt%) at different voltage scan rates, (e) variation of cyclic voltammetry curve at a sweep rate of 100 mVs^{-1}, and (f) galvanometric charging-discharging curve of different samples at a current density of 100 μAg^{-1}

Where C is the specific capacitance (F g^{-1}), I is the discharge current (A), Δt is the discharge time (s), m is the mass of the active material on the working electrode (g), and Δv is the potential change (V) in the discharge process [16]. The estimated values of the specific capacitance for the Cs–MoS$_2$ composites with different concentration of nanofiller is displayed in Table 2. The specific capacitance was increased with the concentration of MoS$_2$ nanofiller, and a specific capacitance as high as 1579 mF/cm^2 was obtained for the Cs–MoS$_2$ (0.5 wt%). The CV and GCD curves for MoS$_2$ nanoflowers are presented in the supplementary figure SF2. The estimated value of the specific capacitance for the MoS$_2$ nanoflowers was found to be 57 F/g. This observation illustrates that incorporating MoS$_2$ nanoflowers to Cs significantly improves the specific capacitances for electrochemical energy storage and broadens new possibilities for rapid electron movement, greatly lowering internal resistance and enhancing electrode electrochemical activity.

MoS$_2$ nanoflower entrapping on the outer layer and interlayers of Cs may be capable of avoiding laminate stacking, which increases the specific surface area [54]. Additionally, the incorporation of MoS$_2$ nanoflower introduces more defects into the polymer matrix. The defects create vacancies that increase the number of electrochemical active sites for interfacial interaction, thereby boosting charge storage performance [55,56]. This could be attributed to the rise of specific capacitance with the continuous addition of MoS$_2$ nanoflower to Cs–MoS$_2$ nanocomposite. The agglomeration in the nanocomposite for the incorporation of a higher concentration of MoS$_2$ nanoflower creates pores on the material's surface, providing more active sites for ion adsorption, the network structure's effective diffusion routes, and the interaction of the components, which could be the reason of the higher capacity of the Cs–MoS$_2$ (0.5 wt%) film [46].

3.6. Electrochemical impedance spectroscopy studies

The electrochemical impedance spectroscopy (EIS) were used to provide a more precise estimate of the electrochemical characteristics of the Cs–MoS$_2$ composites. EIS is an effective and accurate method for investigating the charge transfer processes taking place at the electrochemical cell or functionalized electrode–solution interface. The Nyquist plots (Fig. 6) for each sample show a single semicircle at high frequency followed by a straight line inclined at a CA to the real axis in the low-frequency range [57]. The semicircle pattern at the high-frequency region corresponds to the charge transfer resistance at the electrode and electrolyte interface. The small diameter of the semicircular patterns also indicates lower charge transfer resistance and a relatively high capacitance [58].

The inset of Fig. 6 represents an equivalent circuit used to simulate the EIS data. The circuit consists of an internal resistance (R_s) that accounts for the total resistance resulting from the electrolyte ion transport resistance between the working and reference electrodes, R_{ct} that stands for the charge transfer resistance between the electrolyte and the electrode, Warburg resistance (Z_W), is

Table 2
The specific capacitance of Cs, and Cs–MoS$_2$ nanocomposite.

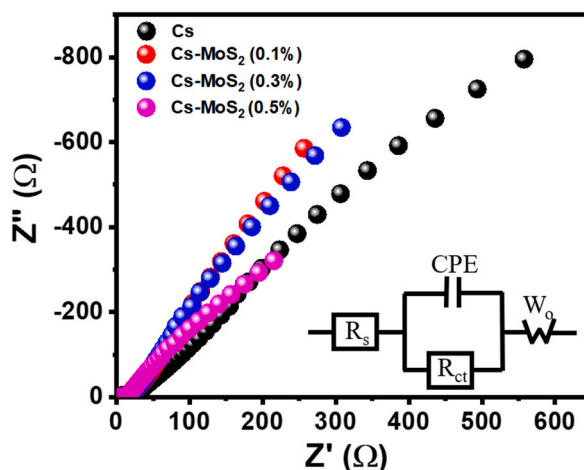| Sample	Specific capacitance (mFg^{-1})
Cs	422
Cs–MoS$_2$ (0.1 %)	429
Cs–MoS$_2$ (0.3 %)	465
Cs–MoS$_2$ (0.5 %)	1579

Fig. 6. Nyquist plots for different samples and the inset shows the equivalent circuit used for simulation.

resistance with the slope of the 45° in the curve, is the result of the frequency dependence of ion diffusion/transport in the electrolyte to the electrode surface and a constant phase element (CPE) instead of an ideal capacitance element for the oxide film. The equivalent series resistance (R_s), the combination of the Ohmic and charge transfer resistances, is represented by the real axis intercept. The ohmic resistance is the combination of the resistance of the electrolyte, the internal resistance of the active material and current collector, as well as the contact resistance among all the materials.

The estimated circuit parameters obtained from the simulation are presented in Table 3. It illustrates the gradual decrease in equivalent series resistance that occurs as the concentration of MoS_2 increases, and the Cs–MoS_2 (0.5 %) electrode exhibits a comparatively low equivalent series resistance (R_s) of 6.97 Ω. The small radius of the semicircle implies that the Faradaic charge transfer resistance (R_{ct}) remains at a very low value as it is determined from the diameter of a semicircle of an impedance plot [59]. As the quantity of MoS_2 nanoflower increased gradually into the Cs–MoS_2 nanocomposites, the R_{ct} value lowered from 9.53 to 2.70 Ohm. Generally, a lower value of R_{ct} is acquired to be ideal double-layer capacitive behavior, and it suggests a faster faradaic reaction with much lower resistance that improves the capacitive performance [60].

Also, the CPE value increased gradually from 0.09 to 4.13 μF due to the incorporation of MoS_2 nanofiller. This improved value of CPE suggests an increase in the electrode/electrolyte interface brought on by faradaic reactions of MoS_2 that also contribute to the observed enhanced electrochemical performance of the Cs–MoS_2 nanocomposites.

The incorporation of MoS_2 significantly improved the electrochemical performance of the Cs matrix. This can be attributed to several factors. The low electrochemical charge transfer resistance of nanocomposite materials demonstrates their high conductivity and efficient charge transportation. The improved specific capacitances of Cs–MoS_2 nanocomposite are generated from the synergistic interaction between Cs and MoS_2 nanoflower. MoS_2 with a larger specific surface area expands the region of the nanocomposite/electrolyte interface functions that are mainly dependent on the pore structure of electrodes. In contrast, the layered structure of MoS_2 lowers the electrolyte ions diffusion length [61]. This expansion of the electroactive zone enhances the specific capacitance. Moreover, the hydrophilicity of MoS_2 enables the ions in the Cs–MoS_2 nanocomposite to migrate to the electrode/electrolyte interface with ease, increasing the action site, reducing the water contamination in the electrode, and producing a high specific capacitance.

4. Conclusions

To sum up, biodegradable Cs–MoS_2 nanocomposites have been synthesized using a simple solution casting technique. The investigation of their structure and surface characteristics reveals an enhanced interaction between Cs and MoS_2, resulting in a decrease in the crystallinity of the composites and the revelation of defects. The UV–vis analysis demonstrates a reduction in the band gap accompanied by an increase in defects, and this observation is corroborated by the Urbach energy analysis attributed to the contribution of MoS_2 loading. The inclusion of MoS_2 enhances surface wettability, as evidenced by the findings of the contact angle study. The Cs–MoS_2 nanocomposites exhibit a specific capacitance that reaches a remarkable 1589 mFg^{-1} at 100 μAg^{-1}, about four times higher than that of Cs alone. The noteworthy reduction in band gap and crystallinity prompts the capture of electrons and ions within the biopolymer matrix, resulting in a significantly improved electrochemical performance. Furthermore, the structural features and the defects induced by sulfur, stemming from the arrangement of stacked MoS_2 nanosheets, contribute to a large surface area, enhanced electrochemical conductivity, and interaction with the –NH functional group provided by the nanofiller. This synergistic effect greatly enhances the electrochemical performance of the nanocomposite. The findings of this study hold the promise of offering a convenient and economical approach to crafting energy storage devices that are ecologically sound.

Table 3
The equivalent circuit parameters of Cs and Cs–MoS$_2$ nanocomposite.

Sample	R$_s$ (Ω)	CPE$_{dl}$ (μF)	R$_{ct}$ (Ω)
Cs	9.25	0.09	9.53
Cs–MoS$_2$ (0.1 %)	7.86	0.82	3.06
Cs–MoS$_2$ (0.3 %)	7.36	1.61	3.00
Cs–MoS$_2$ (0.5 %)	6.97	4.13	2.70

Data availability statement

Data will be made available on request.

CRediT authorship contribution statement

Muhammad Rakibul Islam: Writing – original draft, Writing – review & editing, Supervision, Resources, Project administration, Funding acquisition, Formal analysis, Conceptualization. **Homaira:** Writing – original draft, Investigation, Formal analysis, Data curation. **Eashika Mahmud:** Writing – original draft, Investigation, Formal analysis, Data curation. **Rabeya Binta Alam:** Writing – review & editing, Investigation, Data curation.

Declaration of competing interest

The authors declare that they have no known competing financial interests or personal relationships that could have appeared to influence the work reported in this paper.

Acknowledgments

Appendix A. Supplementary data

Supplementary data to this article can be found online at https://doi.org/10.1016/j.heliyon.2024.e25424.

References

[1] A. Grubler, C. Wilson, N. Bento, B. Boza-Kiss, V. Krey, D.L. McCollum, N.D. Rao, K. Riahi, J. Rogelj, S. De Stercke, J. Cullen, A low energy demand scenario for meeting the 1.5 C target and sustainable development goals without negative emission technologies, Nat. Energy 3 (6) (2018) 515–527.
[2] D. Bresser, D. Buchholz, A. Moretti, A. Varzi, S. Passerini, Alternative binders for sustainable electrochemical energy storage–the transition to aqueous electrode processing and bio-derived polymers, Energy Environ. Sci. 11 (11) (2018) 3096–3127.
[3] Y. Ji, L. Huang, J. Hu, C. Streb, Y.F. Song, Polyoxometalate-functionalized nanocarbon materials for energy conversion, energy storage and sensor systems, Energy Environ. Sci. 8 (3) (2015) 776–789.
[4] M. Chen, Y. Zhang, G. Xing, S.L. Chou, Y. Tang, Electrochemical energy storage devices working in extreme conditions, Energy Environ. Sci. 14 (6) (2021) 3323–3351.
[5] D. Bresser, D. Buchholz, A. Moretti, A. Varzi, S. Passerini, Alternative binders for sustainable electrochemical energy storage–the transition to aqueous electrode processing and bio-derived polymers, Energy Environ. Sci. 11 (11) (2018) 3096–3127.
[6] X. Li, B. Wei, Supercapacitors based on nanostructured carbon, Nano Energy 2 (2) (2013) 159–173.
[7] P. Simon, Y. Gogotsi, Materials for electrochemical capacitors, Nat. Mater. 7 (11) (2008) 845–854.
[8] I.T. Bello, A.O. Oladipo, O. Adedokun, S.M. Dhlamini, Recent advances on the preparation and electrochemical analysis of MoS$_2$-based materials for supercapacitor applications: a mini-review, Mater. Today Commun. 25 (2020) 1064–1072.
[9] I.T. Bello, S.A. Adio, A.O. Oladipo, O. Adedokun, L.E. Mathevula, M.S. Dhlamini, Molybdenum sulfide-based supercapacitors: from synthetic, bibliometric, and qualitative perspectives, Int. J. Energy Res. 45 (9) (2021) 12665–12692.
[10] T. Chao, Y. Hu, X. Hong, Y. Li, Design of noble metal electrocatalysts on an atomic level, Chemelectrochem 6 (2) (2019) 289–303.
[11] X. Guo, G. Zhang, Q. Li, H. Xue, H. Pang, Non-noble metal-transition metal oxide materials for electrochemical energy storage, Energy Storage Mater. 15 (2018) 171–201.
[12] S. Maiti, S.K. Karan, J.K. Kim, B.B. Khatua, Nature-driven bio-piezoelectric/triboelectric nanogenerator as next-generation green energy harvester for smart and pollution-free society, Adv. Energy Mater. 9 (9) (2019) 1803027.
[13] L.F. Chen, Z.H. Huang, H.W. Liang, Q.F. Guan, S.H. Yu, Bacterial-cellulose-derived carbon nanofiber@ MnO$_2$ and nitrogen-doped carbon nanofiber electrode materials: an asymmetric supercapacitor with high energy and power density, Adv. Mater. 25 (34) (2013) 4746–4752.
[14] S.I. Mollik, M.H. Ahmad, R.B. Alam, M.W. Bari, M.R. Islam, Improved thermal, mechanical, and electrochemical performance of bio-degradable starch/reduced graphene oxide nanocomposites, AIP Adv. 11 (9) (2021).
[15] E. Raphael, C.O. Avellaneda, B. Manzolli, A. Pawlicka, Agar-based films for application as polymer electrolytes, Electrochim. Acta 55 (4) (2010) 1455–1459.

[16] Z. Ling, G. Wang, M. Zhang, X. Fan, C. Yu, J. Yang, N. Xiao, J. Qiu, Boric acid-mediated B, N-codoped chitosan-derived porous carbons with a high surface area and greatly improved supercapacitor performance, Nanoscale 7 (12) (2015) 5120–5125.

[17] I. Stepniak, M. Galinski, K. Nowacki, M. Wysokowski, P. Jakubowska, V.V. Bazhenov, T. Leisegang, H. Ehrlich, T. Jesionowski, A novel chitosan/sponge chitin origin material as a membrane for supercapacitors–preparation and characterization, RSC Adv. 6 (5) (2016) 4007–4013.

[18] Y.Y. Wang, B.H. Hou, H.Y. Lü, F. Wan, J. Wang, X.L. Wu, Porous N-doped carbon material derived from prolific chitosan biomass as a high-performance electrode for energy storage, RSC Adv. 5 (118) (2015) 97427–97434.

[19] D. Xu, J. Jin, C. Chen, Z. Wen, From nature to energy storage: a novel sustainable 3D cross-linked chitosan–PEGGE-based gel polymer electrolyte with excellent lithium-ion transport properties for lithium batteries, ACS Appl. Mater. Interfaces 10 (44) (2018) 38526–38537.

[20] D. Zeng, J. Wu, J.F. Kennedy, Application of a chitosan flocculant to water treatment, Carbohydr. Polym. 71 (1) (2008) 135–139.

[21] H.N. Abdelhamid, H.F. Wu, Multifunctional graphene magnetic nanosheet decorated with chitosan for highly sensitive detection of pathogenic bacteria, J. Mater. Chem. B 1 (32) (2013) 3950–3961.

[22] L.S. Anthony, M. Vasudevan, V. Perumal, M. Ovinis, P.B. Raja, T.N.J.I. Edison, Bioresource-derived polymer composites for energy storage applications: Brief review, J. Environ. Chem. Eng. 9 (5) (2021) 105832–105845.

[23] K.J. Huang, Y.J. Liu, Y.M. Liu, L.L. Wang, Molybdenum disulfide nanoflower-chitosan-Au nanoparticles composites based electrochemical sensing platform for bisphenol A determination, J. Hazard Mater. 276 (2014) 207–215.

[24] I.J. Shamsudin, A. Ahmad, N.H. Hassan, H. Kaddami, Bifunctional ionic liquid in conductive biopolymer based on chitosan for electrochemical devices application, Solid State Ionics 278 (2015) 11–19.

[25] I. Stepniak, M. Galinski, K. Nowacki, M. Wysokowski, P. Jakubowska, V.V. Bazhenov, T. Leisegang, H. Ehrlich, T. Jesionowski, A novel chitosan/sponge chitin origin material as a membrane for supercapacitors–preparation and characterization, RSC Adv. 6 (5) (2016) 4007–4013.

[26] M. Deka, A. Kumar, Enhanced electrical and electrochemical properties of PMMA–clay nanocomposite gel polymer electrolytes, Electrochim. Acta 55 (5) (2010) 1836–1842.

[27] L.D. Nguyen, T.C.D. Doan, T.M. Huynh, V.N.P. Nguyen, H.H. Dinh, D.M.T. Dang, C.M. Dang, An electrochemical sensor based on polyvinyl alcohol/chitosan-thermally reduced graphene composite modified glassy carbon electrode for sensitive voltammetric detection of lead, Sensor. Actuator. B Chem. 345 (2021) 130443.

[28] X. Chia, A.Y.S. Eng, A. Ambrosi, S.M. Tan, M. Pumera, Electrochemistry of nanostructured layered transition-metal dichalcogenides, Chem. Rev. 115 (21) (2015) 11941–11966.

[29] M. Pumera, Z. Sofer, A. Ambrosi, Layered transition metal dichalcogenides for electrochemical energy generation and storage, J. Mater. Chem. A 2 (24) (2014) 8981–8987.

[30] A. Sakthivel, A. Chandrasekaran, C. Soosaimanickam, C.Z. Li, S. Alwarappan, WS$_2$ quantum dots harvesting via sonication assisted liquid exfoliation for the electrochemical sensing of xanthine, New J. Chem. 46 (35) (2022) 17066–17072.

[31] A.S. Sethulekshmi, J.S. Jayan, S. Appukuttan, K. Joseph, MoS$_2$: Advanced nanofiller for reinforcing polymer matrix, Phys. E Low-dimens. Syst. Nanostruct. 132 (2021) 114716–114729.

[32] S. Wang, Y. Wang, Y. Liu, T. Zhang, L.B. Kong, Preparation and characterization of nanocomposites of MoS$_2$ nanoflowers and palygorskite nanofibers as lightweight microwave absorbers, Appl. Clay Sci. 2 (11) (2021) 106169–106184.

[33] M. Qin, M. Qi, R. Fan, J. Chen, X. Shi, B. Lin, L. Xi, Y. Wang, K intercalation-assisted Co-doped MoS$_2$ nanoflowers for an efficient hydrogen evolution reaction, precision chemistry 2 (3) (2023) 1490–1503.

[34] I.T. Bello, K.O. Otun, G. Nyongombe, O. Adedokun, G.L. Kabongo, M.S. Dhlamini, Non-modulated synthesis of cobalt-doped MoS$_2$ for improved supercapacitor performance, Int. J. Energy Res. 46 (7) (2022) 8908–8918.

[35] I.T. Bello, K.O. Otun, G. Nyongombe, O. Adedokun, G.L. Kabongo, M.S. Dhlamini, Synthesis, characterization, and supercapacitor performance of a mixed-phase Mn-doped MoS$_2$ nanoflower, Nanomaterials 12 (3) (2022) 490–512.

[36] D. Ailincai, L. Marin, S. Morariu, M. Mares, A.C. Bostanaru, M. Pinteala, B.C. Simionescu, M. Barboiu, Dual crosslinked amino boronated-chitosan hydrogels with strong antifungal activity against Candida planktonic yeasts and biofilms, Carbohydr. Polym. 152 (2016) 306–316.

[37] D. Ailincai, L. Marin, Eco-friendly PDLC composites based on chitosan and cholesteryl acetate, J. Mol. Liq. 321 (2021) 114466–114479.

[38] M.H. Ahmad, R.B. Alam, A. Ul-hamid, S.F.U. Farhad, M.R. Islam, Hydrothermal synthesis of Co$_3$O$_4$ nanoparticles decorated three dimensional MoS$_2$ nanoflower for exceptionally stable supercapacitor electrode with improved capacitive performance, J. Energy Storage 47 (2022) 1–12.

[39] X. Feng, X. Wang, W. Xing, K. Zhou, L. Song, Y. Hu, Liquid-exfoliated MoS$_2$ by chitosan and enhanced mechanical and thermal properties of chitosan/MoS$_2$ composites, Compos. Sci. Technol. 93 (2014) 76–82.

[40] A.A. Menazea, A.M. Ismail, N.S. Awwad, H.A. Ibrahium, Physical characterization and antibacterial activity of PVA/Chitosan matrix doped by selenium nanoparticles prepared via one-pot laser ablation route, J. Mater. Res. Technol. 9 (5) (2020) 9598–9606.

[41] M. Imani, L. Radmanesh, A. Tadjarodi, Synthesis and study of the pseudocapacitive behavior of heterojunctional NiTiO$_3$-based chitosan nanocomposite, J. Phys. Chem. Solid. 139 (2020) 109309.

[42] X. Feng, X. Wang, W. Xing, K. Zhou, L. Song, Y. Hu, Liquid-exfoliated MoS$_2$ by chitosan and enhanced mechanical and thermal properties of chitosan/MoS$_2$ composites, Compos. Sci. Technol. 93 (2014) 76–82.

[43] J. Ji, H. Xiong, Z. Zhu, L. Li, Y. Huang, X. Yu, Fabrication of polypyrrole/chitosan nanocomposite aerogel monolith to remove Cr (VI), J. Polym. Environ. 26 (2018) 1979–1985.

[44] E.M. Hussein, W.M. Desoky, M.F. Hanafy, O.W. Guirguis, Effect of TiO$_2$ nanoparticles on the structural configurations and thermal, mechanical, and optical properties of chitosan/TiO$_2$ nanoparticle composites, J. Phys. Chem. Solid. 152 (2021) 109983–109998.

[45] D. Merki, S. Fierro, H. Vrubel, X. Hu, Amorphous molybdenum sulfide films as catalysts for electrochemical hydrogen production in water, Chem. Sci. 2 (7) (2011) 1262–1267.

[46] Z. Chen, K. Saito, T. Tanaka, M. Nishio, M. Arita, Q. Guo, Low temperature growth of europium doped Ga$_2$O$_3$ luminescent films, J. Cryst. Growth 430 (2015) 28–33.

[47] K.A. Hurayra–Lizu, M.W. Bari, F. Gulshan, M.R. Islam, GO based PVA nanocomposites: tailoring of optical and structural properties of PVA with low percentage of GO nanofillers, Heliyon 7 (5) (2021) 1-18.

[48] B. Choudhury, A. Choudhury, Oxygen defect dependent variation of band gap, Urbach energy and luminescence property of anatase, anatase–rutile mixed phase and of rutile phases of TiO$_2$ nanoparticles, Phys. E Low-dimens. Syst. Nanostruct. 56 (2014) 364–371.

[49] M. Nagaraja, P. Raghu, H.M. Mahesh, J. Pattar, Structural, optical and Urbach energy properties of ITO/CdS and ITO/ZnO/CdS bi-layer thin films, J. Mater. Sci. Mater. Electron. 32 (2021) 8976–8982.

[50] B. Ghosh, F. Guzmán-Olivos, R. Espinoza-González, Plasmon-enhanced optical absorption with graded bandgap in diamond-like carbon (DLC) films, J. Mater. Sci. 52 (1) (2017) 218–228.

[51] M.I. Mohammed, W. Jilani, A. Bouzidi, H.Y. Zahran, M. Jalalah, F.A. Harraz, I.S. Yahia, Synthesis, optical properties, and impedance spectroscopy of Na$_2$TeO$_3$ doped polyvinyl alcohol as novel polymeric electrolyte films, Opt. Quant. Electron. 53 (6) (2021) 280.

[52] C.S. Lim, K.H. Teoh, C.W. Liew, S. Ramesh, Capacitive behavior studies on electrical double layer capacitor using poly (vinyl alcohol)–lithium perchlorate-based polymer electrolyte incorporated with TiO$_2$, Mater. Chem. Phys. 143 (2) (2014) 661–667.

[53] Y. Chen, X. Zhu, D. Yang, P. Wangyang, B. Zeng, H. Sun, A novel design of poly (3, 4-ethylenedioxythiophene): poly (styrenesulfonate)/molybdenum disulfide/ poly (3, 4-ethylenedioxythiophene) nanocomposites for fabric micro-supercapacitors with favourable performances, Electrochim. Acta 298 (2019) 297–304.

[54] A. Ehsani, H. Parsimehr, H. Nourmohammadi, R. Safari, S. Doostikhah, Environment-friendly electrodes using biopolymer chitosan/poly ortho aminophenol with enhanced electrochemical behavior for use in energy storage devices, Polym. Compos. 40 (12) (2019) 4629–4637.

[55] H. Wang, X. Xu, A. Neville, Facile synthesis of vacancy-induced 2H-MoS$_2$ nanosheets and defect investigation for supercapacitor application, RSC Adv. 11 (42) (2021) 26273–26283.

[56] W. Lu, L. Yan, W. Ye, J. Ning, Y. Zhong, Y. Hu, Defect engineering of electrode materials towards superior reaction kinetics for high-performance supercapacitors, J. Mater. Chem. A 10 (29) (2022) 15267–15296.

[57] W. Teng, Q. Zhou, X. Wang, H. Che, P. Hu, H. Li, J. Wang, Hierarchically interconnected conducting polymer hybrid fiber with high specific capacitance for flexible fiber-shaped supercapacitor, Chem. Eng. J. 390 (2020) 124569.

[58] I.R. Rodrigues, M.M. de Camargo Forte, D.S. Azambuja, K.R. Castagno, Synthesis and characterization of hybrid polymeric networks (HPN) based on polyvinyl alcohol/chitosan, React. Funct. Polym. 67 (8) (2007) 708–715.

[59] A. Ehsani, M. Bigdeloo, F. Assefi, M. Kiamehr, R. Alizadeh, Ternary nanocomposite of conductive polymer/chitosan biopolymer/metal organic framework: synthesis, characterization and electrochemical performance as effective electrode materials in pseudo capacitors, Inorg. Chem. Commun. 115 (2020) 107885–107899.

[60] L. Zhu, F. Shen, R.L. Smith Jr., X. Qi, High-performance supercapacitor electrode materials from chitosan via hydrothermal carbonization and potassium hydroxide activation, Energy Technol. 5 (3) (2017) 452–460.

[61] F. Alvi, M.K. Ram, P.A. Basnayaka, E. Stefanakos, Y. Goswami, A. Kumar, Graphene–polyethylenedioxythiophene conducting polymer nanocomposite-based supercapacitor, Electrochim. Acta 56 (25) (2011) 9406–9412.